



Effect of cation doping on the electrochemical properties of Li_2MoO_3 as a promising cathode material for lithium-ion battery

Rui Teng¹ · Hai-Tao Yu¹ · Chen-Feng Guo¹ · Xiao-dong Wang² · Ying-Jie Qiao² · Ying Xie¹ · Ting-Feng Yi^{3,4}

Received: 23 March 2020 / Revised: 24 April 2020 / Accepted: 3 May 2020 / Published online: 30 May 2020
© Springer-Verlag GmbH Germany, part of Springer Nature 2020

Abstract

A series of cation-doped Li_2MoO_3 materials were successfully prepared by a facile method. The experimental characterizations showed that the incorporation of metal cations can change the structures of Li_2MoO_3 materials. In addition, $\text{Li}_2\text{Mo}_{0.96}\text{M}_{0.04}\text{O}_3$ materials have higher structural stabilities and electrical conductivities in comparison to the pristine sample, which results in a much improved electrochemical performance. The initial discharge capacities are respectively 246.87, 256.92, 255.38, 271.12, and 261.25 mAh g^{-1} for Li_2MoO_3 , $\text{Li}_2\text{Mo}_{0.96}\text{Zn}_{0.04}\text{O}_3$, $\text{Li}_2\text{Mo}_{0.96}\text{Mg}_{0.04}\text{O}_3$, $\text{Li}_2\text{Mo}_{0.96}\text{Cr}_{0.04}\text{O}_3$, and $\text{Li}_2\text{Mo}_{0.96}\text{La}_{0.04}\text{O}_3$. $\text{Li}_2\text{Mo}_{0.96}\text{La}_{0.04}\text{O}_3$ has the best performance, and it can deliver a specific capacity of 149.89 mAh g^{-1} at the 50th cycle at a charge/discharge current density of 34 mA g^{-1} . Our experiments have identified the promising role of cation doping and offered some important information for the design and optimization of Li_2MoO_3 -based cathode materials.

Keywords Cation doping · Li_2MoO_3 · Lithium-ion battery

Introduction

Rechargeable lithium ion battery (LIB) has gradually become the main power source of portable products due to its high energy density, long cycle life, and low cost. However, with its application in electric vehicles, hybrid electric vehicles, and smart grids, demands for higher energy density LIB are urgently required [1]. In recent years, the development of high

specific capacity and novel lithium ion battery cathode materials has received great attentions. In comparison to conventional cathode materials like olivine-type LiFePO_4 [2] and $\text{Li}_3\text{V}_2(\text{PO}_4)_3$ [3] and silicate-based oxides Li_2MSiO_4 (M=Fe and Mn) [4, 5], manganese-based-layered lithium-rich cathode (LLRC) material with the formula of $x\text{Li}_2\text{MnO}_3 \cdot (1-x)\text{LiMO}_x$ ($0 < x < 1$) was focused on due to its specific capacity higher than 250 mAh g^{-1} [6]. However, this material generally has a low lithium ion migration rate, a large irreversible capacity in the first circle, a severe voltage and capacity fading, and the oxygen release issue, which hinders its practical application [7].

Therefore, it is necessary to find alternative materials to overcome these inherent defects. In recent years, a strategy to increase the theoretical capacity of the cathode and to suppress the oxygen evolution issue is constructing new materials with other Li_2MO_3 (M = Ru, Ir, Sn, Mo) components [8–12]. Since lithium-rich Li_2MO_3 phase can exchange more than one lithium during cycling, the capacity of the material can exceed 300 mAh g^{-1} [13, 14]. According to previous reports, it was confirmed that Li_2MoO_3 undergoes a multi-electron redox reaction and its theoretical capacity is 339 mAh g^{-1} without oxygen release [15–17]. The existence of the $\text{Mo}^{4+}/\text{Mo}^{6+}$ redox pair can avoid many structural problems caused by oxygen evolution [18]. These unique advantages make Li_2MoO_3 a promising building block for the design of next-generation

✉ Xiao-dong Wang
wangxiaodong@hrbeu.edu.cn

✉ Ying Xie
xiying@hlju.edu.cn

✉ Ting-Feng Yi
tfyihit@163.com

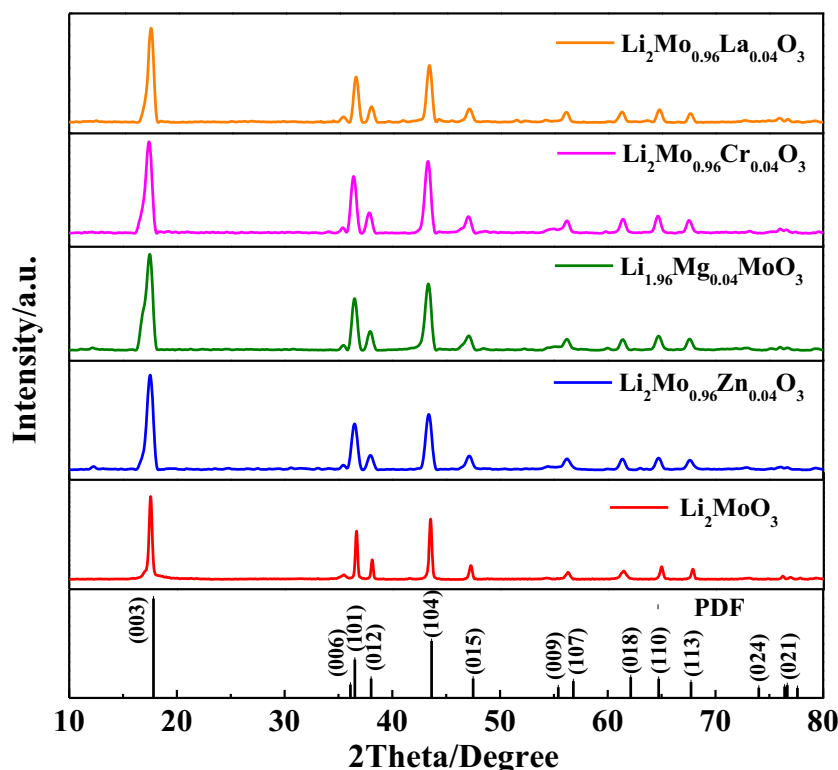
¹ Key Laboratory of Functional Inorganic Material Chemistry, Ministry of Education, School of Chemistry and Materials Science, Heilongjiang University, Harbin 150080, People's Republic of China

² College of Material Science and Chemical Engineering, Harbin Engineering University, Harbin 150001, People's Republic of China

³ School of Resources and Materials, Northeastern University at Qinhuangdao, Qinhuangdao 066004, People's Republic of China

⁴ Institute of Advanced Electrochemical Energy, School of Materials Science and Engineering, Xi'an University of Technology, Xi'an 710048, Shanxi, People's Republic of China

Fig. 1 XRD patterns for LMO, LMZO, LMMO, LMCO, and LMLO samples



cathode materials. However, the preparation difficulty and the poor conductivity of Li_2MoO_3 must be solved before its practical application [10].

In recent years, many strategies have been applied to improve the electrochemical properties of the lithium-rich materials [6, 19, 20]. However, anion and cation doping is considered to be the most simple, effective, and economical method to achieved this goal [21, 22]. The electrochemical performance of $\text{Li}(\text{Li}_{0.2}\text{Ni}_{0.15+0.5z}\text{Co}_{0.1}\text{Mn}_{0.55-0.5z})\text{O}_{2-z}\text{F}_z$ was investigated by Kang and co-workers, and the results show that F doping can improve the capacity retention of the material [23]. The reasons were suggested to be that fluorine doping decreases the cell impedance for Li^+ diffusion, and it stabilizes the crystal structure by suppressing the formation of oxygen vacancies in the first charging process. Sung Park et al. have reported that iron ions were doped into $(1-x)\text{Li}_2\text{MoO}_3-x\text{LiFeO}_2$ materials, and the incorporation of iron ions stabilizes the crystal structure of the material and inhibits the dissolution of Mo(VI) [24]. According to previous literatures, Fe^{2+} [25, 26], Mg^{2+} [20, 27], Zn^{2+} [28, 29], and Cr^{3+} [30, 31] elements have been widely used to stabilize the crystal structure of Mn-based LLRC and improve their conductivity. However, this impact on Li_2MoO_3 is still unknown and deserves further considerations. It is expected that there is still an undeveloped cationic doping library, which also has a positive contribution on the structure and electrochemical performance of Li_2MoO_3 [17]. Therefore, in the present manuscript, four typical cations, i.e., Zn^{2+} , Mg^{2+} , Cr^{3+} , and La^{3+} , were doped

into Li_2MoO_3 materials. Our experiments have revealed the origin of the doping effect, which provides some useful information for the modification and design of relevant Li_2MoO_3 materials in the future.

Experimental section

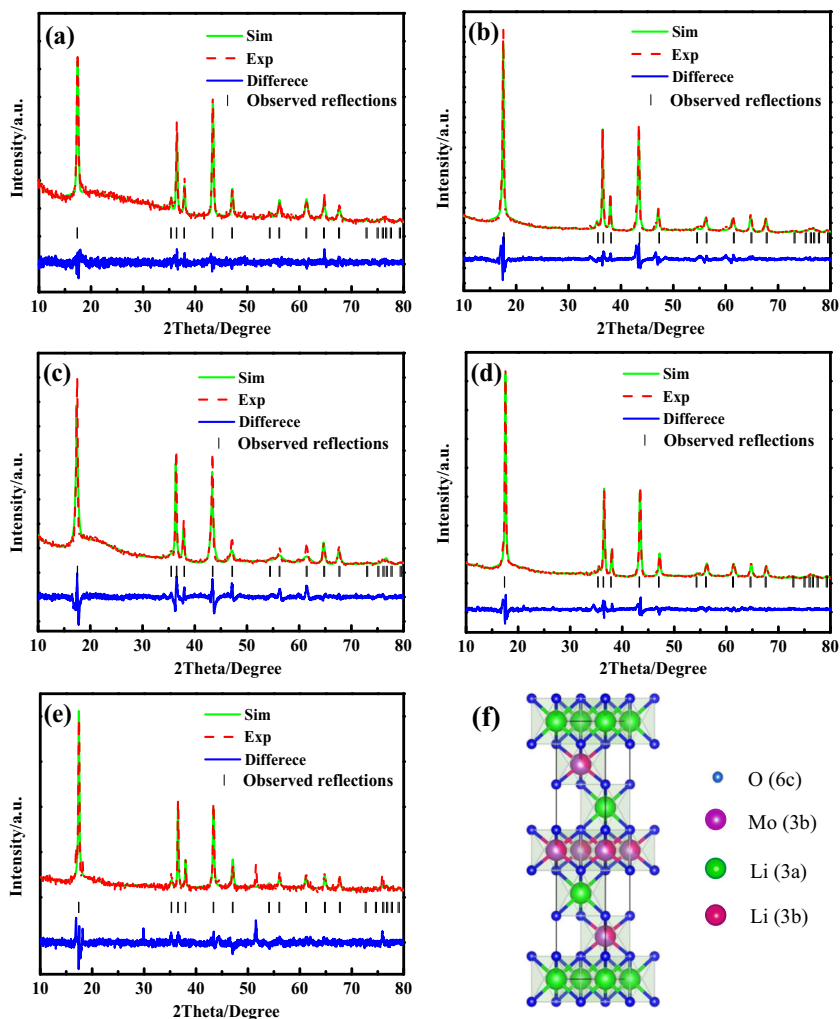
Sample preparation

All chemical reagents are of the A.R. grade and used without further purification. The pristine and cation-doped samples were synthesized by a facile molten salt method [32, 33]. First, a stoichiometric amount of Li_2CO_3 (5% excess), MoO_2 , $(\text{CH}_3\text{COO})_2\text{Zn}\cdot 2\text{H}_2\text{O}$, $\text{Mg}(\text{NO}_3)_2\cdot 6\text{H}_2\text{O}$, $(\text{CH}_3\text{COO})_3\text{Cr}$, $\text{La}(\text{NO}_3)_3\cdot 6\text{H}_2\text{O}$, KCl, and NaCl was

Table 1 Lattice constants calculated from Rietveld refinement for different samples.

	LMO	LMZO	LMMO	LMCO	LMLO
a(Å)	2.8635	2.8640	2.8587	2.8619	2.8688
c(Å)	15.0879	15.0922	15.1278	15.0409	15.1543
I(003)/I(104)	1.373	1.709	1.447	1.272	1.652
R_{wp}	6.74%	15.47%	11.69%	11.56%	5.76%

Fig. 2 Rietveld analysis for **a** LMO, **b** LMZO, **c** LMMO, **d** LMCO, **e** LMLO, and **f** refinement model



dispersed in distilled water, and the solution was evaporated to dryness at 80 °C in a water bath. The mixture was calcined at 700 °C for 7 h in a tube furnace with a H₂/Ar (5:95 v/v) flow

and naturally cooled down to room temperature. The resulting sample was washed with distilled water to remove KCl and NaCl. Five samples, Li₂MoO₃, Li₂Mo_{0.96}Zn_{0.04}O₃,

Fig. 3 SEM images for **a** MoO₂, **b** LMO, **c** LMZO, **d** LMMO, **e** LMCO, and **f** LMLO samples

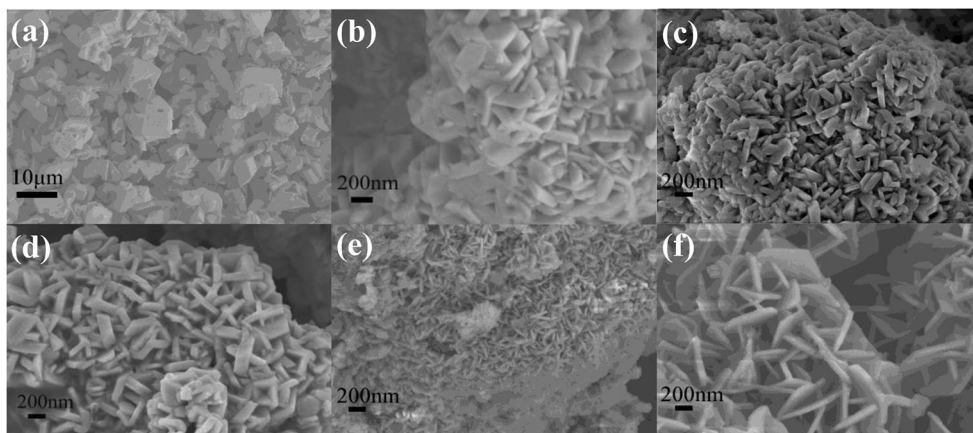
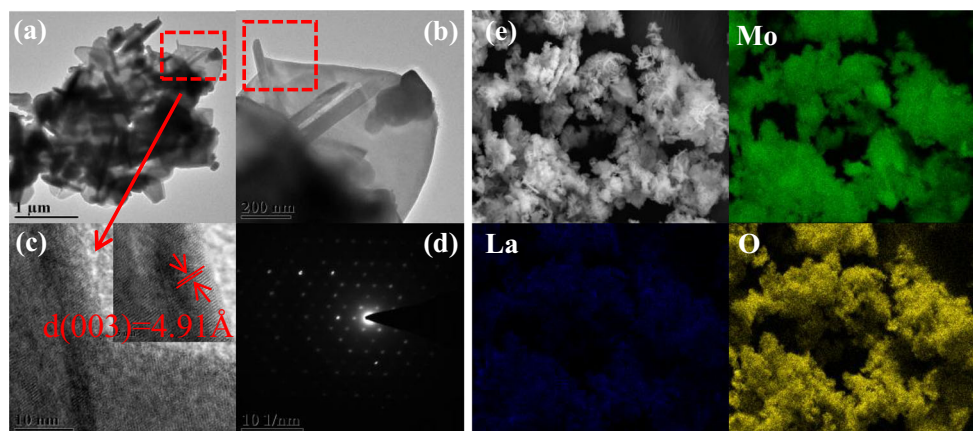


Fig. 4 **a** Low-resolution and **b** high-resolution TEM images of LMLO sample. **c** Lattice fringes and **d** diffractions of selected area **e** EDS mapping for LMLO



$\text{Li}_{1.96}\text{Mg}_{0.04}\text{MoO}_3$, $\text{Li}_2\text{Mo}_{0.96}\text{Cr}_{0.04}\text{O}_3$, and $\text{Li}_2\text{Mo}_{0.96}\text{La}_{0.04}\text{O}_3$, were obtained and labeled as LMO, LMZO, LMMO, LMCO, and LMLO, respectively.

Material characterization and electrochemical testing

X-ray powder diffraction (XRD) patterns were recorded by a Bruker D8 instrument. The morphologies of the samples were measured by a Hitachi S-4800 scanning electron microscopy (SEM) and a JEOL 2100 transmission electron microscopy (TEM). The elemental compositions were characterized by using the energy-dispersive spectroscopy (EDS) (Oxford INCA, Britain). X-ray photoelectron spectroscopy (XPS) analysis was performed by using an ESCALab 250 system. All samples were tested in a half cell with Li metal as the counter anode, and Celgard 2400 membrane was used as the separator. The active materials (80 wt%), super-P carbon black (10 wt%) and polyvinylidene fluorides (10 wt%) were dissolved in *N*-methyl-2-pyrrolidinone (NMP) to form a slurry, which was then pasted on the surface of an aluminum foil. After the foil was dried under a vacuum condition at 110 °C for 12 h, it was cut into circle sheets with a diameter of 14 mm. The sheets were further pressed at 3 MPa to form the final cathode. The active materials loaded on the cathode were

about 0.91 mg cm^{-2} . CR2025 coin cells were assembled in an argon-filled glovebox, in which the moisture and oxygen concentrations were both below 0.1 ppm. The electrolyte was 1 M LiPF_6 solution solved in a mixture of ethylene carbonate (EC) and diethyl carbonate (DEC) (EC/DEC, volume ratio, 1:1). The loading of the active materials is 0.48–0.88 mg, and the 1 C rate corresponds to a current density of 340 mA g^{-1} . The charge and discharge behaviors of the half-cells were recorded between 1.5 and 4.3 V (vs. Li^+/Li) at room temperature by using a LAND CT2001A system under constant current conditions. Electrochemical impedance spectroscopy (EIS) study was conducted by using a Princeton P4000 electrochemical working station over a frequency range from 0.01 Hz to 100 kHz at a potentiostatic signal amplitude of 5 mV. Cyclic voltammetry (CV) tests were carried out on a CHI 1000C electrochemical workstation with a voltage between 1.5 and 4.3 V and a scanning rate of 0.1 mV s^{-1} .

Results and discussion

Figure 1 shows the XRD patterns of LMO, LMZO, LMMO, LMCO, and LMLO. The peaks of the five samples can be indexed into the $\alpha\text{-NaFeO}_2$ structure with a $R\bar{3}_m$ space group

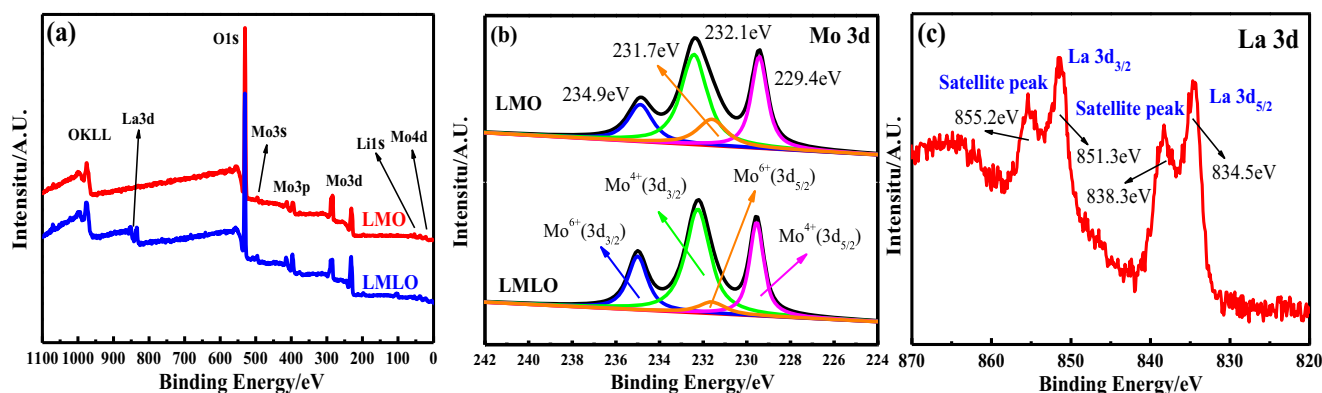


Fig. 5 XPS spectrum for **a** LMO and LMLO sample, **b** Mo3d, and **c** La 3d bands

(PDF#88-0303) [10]. No obvious impurities or secondary phase can be observed, while the sharp and well-defined peaks imply that five samples are well crystallized. This result also suggested that the doping elements were successfully introduced into Li_2MoO_3 . The lattice parameters of all samples are calculated via the Rietveld refinement, and the data are summarized in Table 1. The results clearly showed that a and c for pristine Li_2MoO_3 are 2.863(5) and 15.087(9) Å, while the lattice parameters of Zn^{2+} , Mg^{2+} , and La^{3+} -doped samples are slightly expanded. Owing to the expanded layer distance, it can be expected that the diffusion of lithium within lithium layer will be improved. The lattice parameters of the sample after Cr^{3+} doping decreased slightly [34], but the incorporation of the cation disorder material Cr can be uniformly distributed between the metal layers, resulting in an increase in Li^+ diffusivity [35]. Furthermore, it can be found that different from the conventional Mn-based LLRC materials, no peaks appear between 20° and 25° for all investigated samples, and the intensity ratios of the (003)/(104) peaks are large. These features suggested that the antisite arrangements between Li_{3a} and Mo_{3b} are scarce [10, 18]. On the other hand, a clear splitting can be observed for the (006)/(101) pair and the (018)/(110) one, indicating that the five samples have an ideal layered structure [10, 18]. Zn^{2+} , Mg^{2+} , Cr^{3+} , and La^{3+} can be successfully doped into the lattice of Li_2MoO_3 without affecting the diffraction pattern and causing any impurities.

To determine the lattice parameters and atomic positions, Rietveld refinements were performed and the results are displayed in Fig. 2. Based on the refinement model in Fig. 2f, the atomic positions for different species were determined. Our calculation confirmed that lithium occupies 3a and 3b sites, while molybdenum and doping elements are located at 3b site. Oxygen takes the 6c sites. The occupation ratio of the 3b site Li and Mo is very close to 1:2, implying that Mo/Li disordering is mainly restricted within the transition metal layer.

Figure 3 is SEM images of the MoO_2 precursor, LMO, and four M-doped LMO samples. It can be seen from Fig. 3a that the MoO_2 precursor is an irregular block structure with a diameter of about 2–7 μm . Due to the incorporation of metal cations, the morphology of the samples changes significantly, and the synthesized LMO, LMZO, LMMO, LMCO, and LMLO samples are mainly composed of stacking flakes. Compared with the LMO pristine sample (Fig. 3b), the average particle size and the flake thickness of the LMZO, LMMO, and LMCO materials all decreased. Especially for the LMCO sample, its size was even reduced to tens of nanometers, which suggests that the diffusion dynamics of lithium of this sample should be good [36–38]. On the contrary, for the LMLO sample, its width increases significantly while its thickness decreases to ~ 20 nm. As a result, the wide and ultrathin nano-sheets are formed. More importantly, the stacking of the large nano-sheet leads to very large void spaces (Fig. 3f),

which is very helpful for the penetration of the electrolyte and the enhancement of the interfacial contacts. As a result, the surface area of the LMLO sample should be the largest, which will lead to an excellent rate capability [39].

To further reveal the structural details of the material, TEM images of LMLO samples were obtained. As shown in Fig. 4a, it can be proved that the La^{3+} -doped material is composed of a series of nano-sheet, which is consistent with the SEM results. In addition, the calculated lattice fringes of the LMLO sample corresponding to the (003) crystal facets are ~ 0.491 nm. The electron diffraction pattern of the selected area shows that the prepared sample is simple crystal with a good hexagonal structure. Figure 4 b shows the EDS mapping of the LMLO sample. It can be seen that the elements of La, Mo, and O are evenly distributed, which proves that lanthanum ions have entered the lattice. Compared with traditional solid-state synthesis, the introduction of KCl and NaCl as molten salts will provide a liquid environment at high temperature to facilitate the diffusion of different ions, leading to the specific morphology and the even distribution of the element. These features are favorable for boosting the electrochemical performance of the materials.

XPS is a powerful tool for analyzing the oxidation state of ions and the elemental composition. Figure 5 a shows the full spectrum of different samples with the peaks corresponding to Li 1s, Mo 3s, Mo 3p, Mo 3d, Mo 4d, and O 1s bands. The high-resolution XPS spectrum for molybdenum in Fig. 5b clearly shows that $3d_{5/2}$ and $3d_{3/2}$ bands of Mo^{4+} are located at 229.4 and 232.1 eV, while those of Mo^{6+} are at 231.7 and 234.9 eV. This observation is coincident with previous literatures [40–42] and also confirms the surface oxidation of pristine Li_2MoO_3 in air [43, 44]. However, it is interesting to note that the positions of the characteristic peaks are nearly unchanged. When La^{3+} is incorporated, the strength of Mo^{6+} $3d_{5/2}$ at 231.7 eV decreases obviously. Figure 5 c is a high-

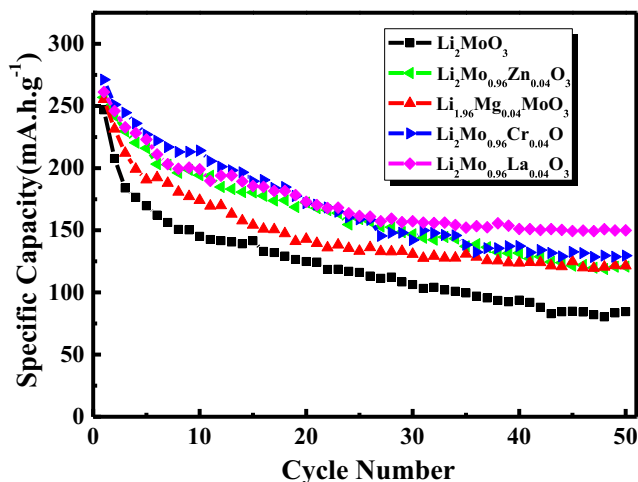


Fig. 6 Cyclic performance of different samples at current density of 34 mA g^{-1}

resolution XPS spectrum of La 3d band. It can be seen that the spectrum is mainly composed of two double peaks distributed near 834.5 eV and 851.3 eV, which belong to the La 3d_{5/2} and La 3d_{3/2} bands, respectively. The peaks at 838.3 eV and 855.2 eV are the oscillating satellite peaks for La 3d_{5/2} and La 3d_{3/2} bands [45]. This signature was also confirmed in La-doped TiO₂ materials [46].

The cyclic performance of different samples is depicted in Fig. 6. It can be noted that the initial discharge capacity of the pristine sample is 246.87 mA h g⁻¹, and it retains at 84.49 mA h g⁻¹ at the 50th cycle. The capacity retention is 34.22%. The

continuous capacity decrease during cycling may be attributed to two possible reasons, the irreversible crystalline to amorphous transition [17] and the dissolution of Mo⁶⁺ at 4.3 V [47]. However, due to cation doping, the initial discharge capacities for LMZO, LMMO, LMCO, and LMLO samples increase significantly to 256.92, 255.38, 271.12, and 261.25 mA h g⁻¹. The capacity retentions are 47.01%, 47.55%, 47.81%, and 57.38%. Our results confirmed that La³⁺ doping increases the cyclic stability of the compounds. Since Mo⁴⁺ has much smaller ionic radius (65 pm) with respect to La³⁺ (103.2 pm), the introduction of La³⁺ at Mo⁴⁺ site will increase

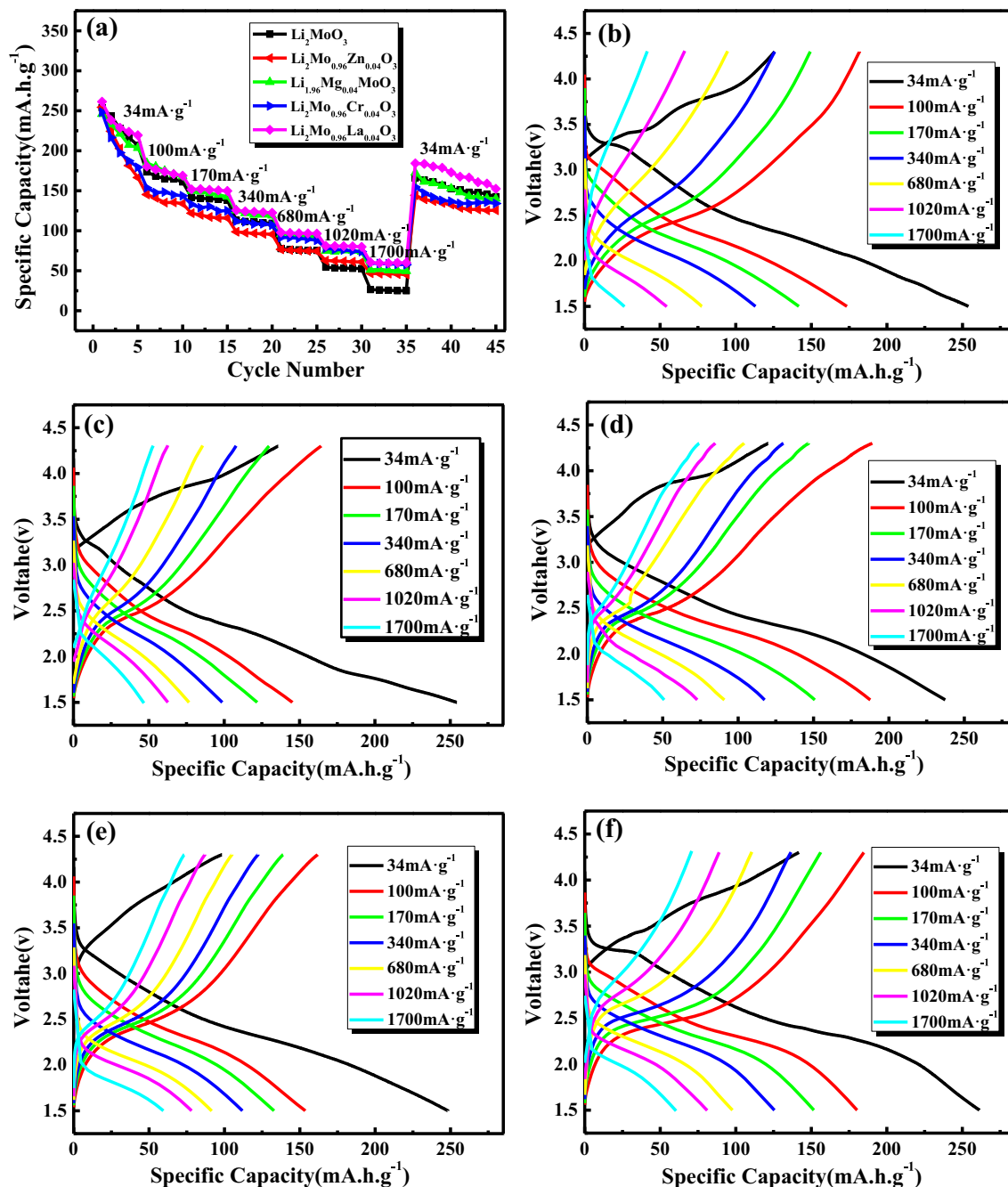


Fig. 7 a Rate capability of different samples and charge/discharge curves for b LMO, c LMZO, d LMMO, e LMCO, and f LMLO samples

the inter-planar spacing, which was confirmed by the XRD refinement above. This feature suggested that lithium ion diffusion in LMLO should be higher than pristine LMO sample.

The rate capability of different samples is shown in Fig. 7a. The charge current density is 34 mA g^{-1} , while the discharge current density ranges from 34 to 1700 mA g^{-1} . It can be found that the discharge capacity of each sample gradually decreases with the increase of current density. This result is correlated to the redox polarization under different current density. Compared with the pristine sample, the specific capacities of all doped samples at high current density

conditions are much higher, indicating that the redox polarization will decrease significantly due to cation doping. From the viewpoint of band structure, partial substitution of molybdenum by La^{3+} ions will change the valence state of the species in the materials, leading to varied oxidation states for Mo ions. Due to partial Mo^{5+} ions in LMLO, partially filled energy bands are thus expected. Therefore, it can be deduced that the electronic conductivity of LMLO should be improved. On the other hand, the larger radius of La^{3+} expands the (001) layer distance, leading to a lower charge transfer resistance. Therefore, at a current density of 1700 mA g^{-1} , LMLO can

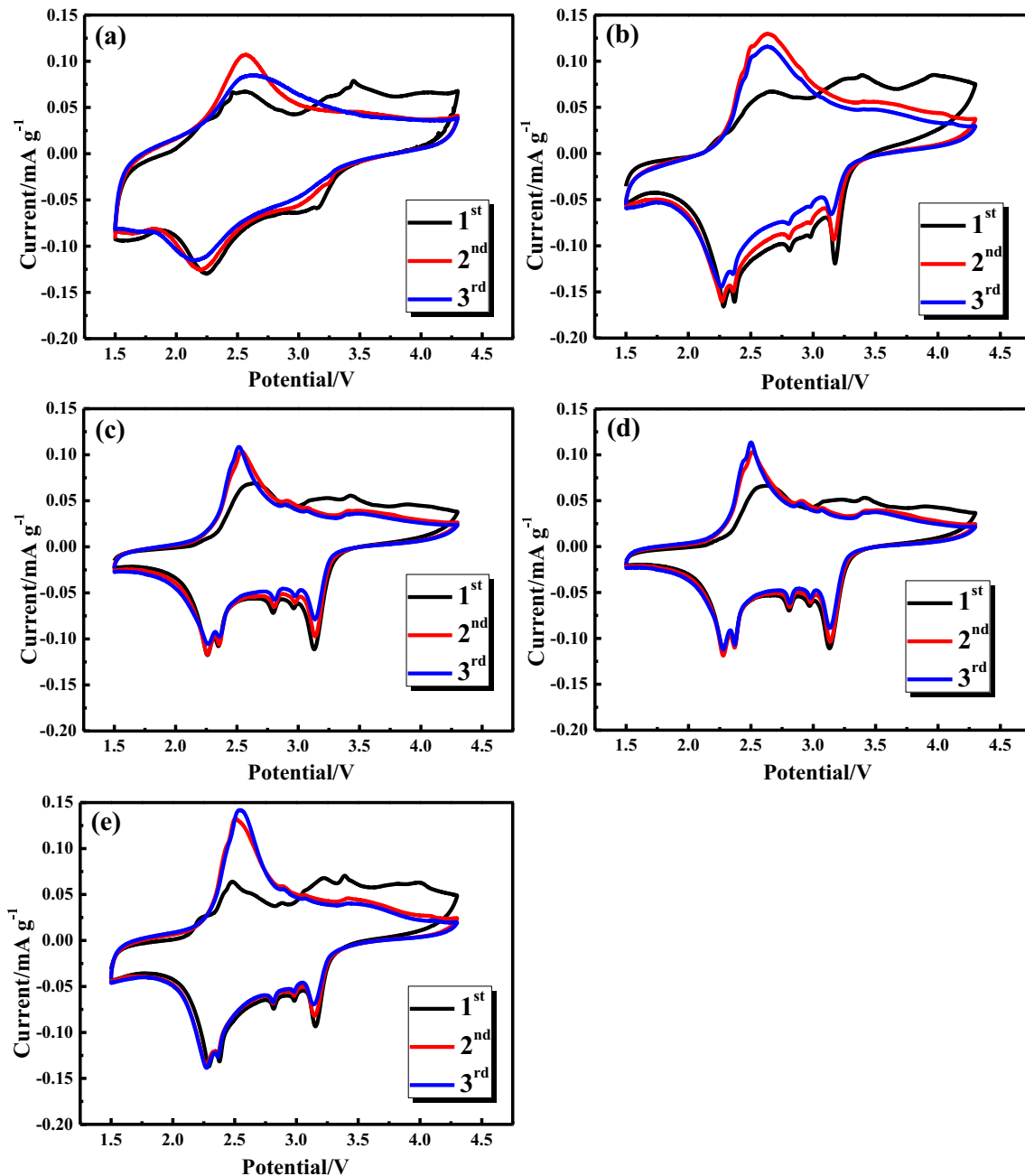


Fig. 8 Cyclic voltammeteries (CVs) for a LMO, b LMZO, c LMMO, d LMCO, and e LMLO samples

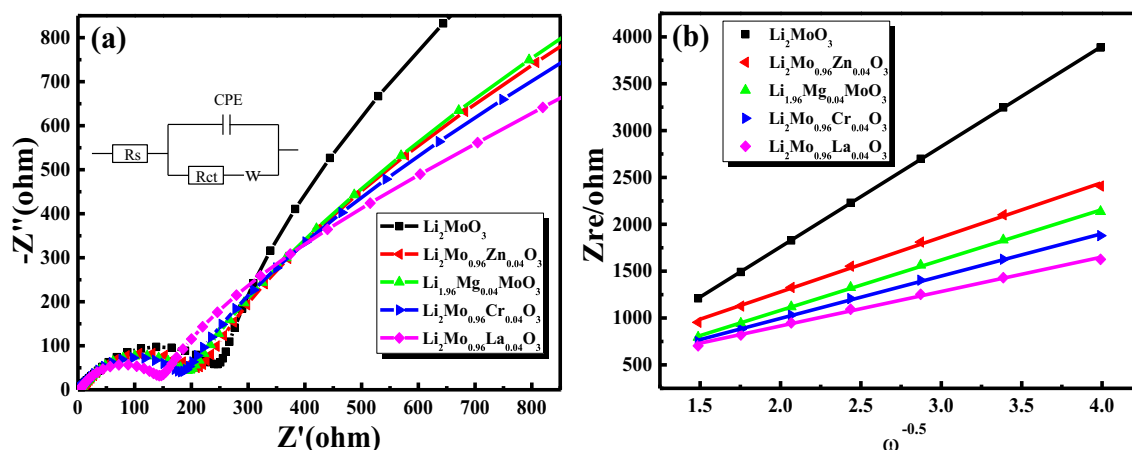


Fig. 9 **a** EIS patterns of different samples and **b** Z_{re} as a function of $\omega^{-0.5}$ at low-frequency region

still deliver a specific capacity of 60.44 mAh g^{-1} , which is also the highest among all samples. Figure 7 b–f are the charge and discharge curves of different samples. For pristine Li_2MoO_3 , no obvious presence of voltage plateau was observed at low current density condition. When the current density increases to 100 mA g^{-1} , it can be observed that a small voltage platform appears at 2.3 V. However, the situation in LMLO samples is different, and it can be found that the plateau region at 2.3 V is expanded obviously. This is responsible for the increase discharge capacities of the sample. Our experiments also suggested that trivalent cation doping seem to be superior to the divalent cation doping.

The cyclic voltammeteries (CVs) are plotted in Fig. 8. It can be observed that two redox pairs for pristine sample are located at 2.75/2.25 V and 3.5/3.15 V, and the high potential oxidation peak is nearly disappeared in subsequent cycles. This phenomenon is reported to be related to the irreversible crystalline to amorphous transformation of the material [17]. However, with the doping of cation, the materials exhibit an entirely different behavior from previous reports [16, 24, 47]. The two redox pairs become more clear and strengthened gradually due to the doping. In comparison to the pristine sample, the enhanced structural stability of the doped materials will suppress the irreversible phase transformation and increase the reversibility of the electrochemical reactions. Furthermore, thanks to the complex charge compensation condition caused by the non-equivalent doping (M^{2+} or M^{3+}), partial Mo ions will deviate from their normal oxidation states, and the formation of $\text{Mo}^{(4+\delta)+}$ species becomes

possible. This can also be verified by the plateau observed in the charge discharge curve of Fig. 7. Therefore, multiple small but reversible redox pairs appear in the CV curves. For the LMLO sample, the potential difference between its oxidation and reduction peaks is significantly reduced, while its peak current is also the largest. Therefore, LMLO sample has an excellent activity and reversibility.

EIS measurements were performed and shown in Fig. 9a. The Nyquist plots are composed of two parts, a depressed semicircle in the high-frequency region and a straight line in the low-frequency region. The former is related to the charge transfer resistance (R_{ct}) at the particle/electrolyte interface, while the latter corresponds to a semi-infinite Warburg diffusion process [48, 49]. It can be found that the R_{ct} value of LMLO is much smaller than those of LMO, LMZO, LMMO, and LMCO samples. This result identified that La dopant does increase the electrochemical activity of the materials. Furthermore, the diffusion coefficient of lithium ions (D_{Li}) can also be calculated by

$$Z_{re} = R_{ct} + R_s + \sigma\omega^{-\frac{1}{2}} \quad (1)$$

$$D_{\text{Li}} = \frac{2R^2T^2}{A^2n^4F^4C_{\text{Li}}\sigma^2} \quad (2)$$

where $R, T, A, n, F, D_{\text{Li}}$ are the gas constant, the absolute temperature, the surface area of the cathode, the number of electrons transferred in the half-reaction, the Faraday constant, and the concentration of lithium ion in solid, respectively,

Table 2 EIS fitting data for different samples

Samples	LMO	LMZO	LMMO	LMCO	LMLO
R_{ct}/Ω	1071.138	583.078	537.957	452.132	367.904
$D_{\text{Li}}/\text{cm}^2 \text{ s}^{-1}$	6.66×10^{-17}	2.25×10^{-16}	2.64×10^{-16}	3.74×10^{-16}	5.64×10^{-16}

while σ denotes as the Warburg factor. As reported previously, the relationship between the real part of impedance (Z_{re}) and σ_w is governed by Eq. (1) [49, 50]. Z_{re} as a function of the reciprocal root square of the lower angular frequencies ($\omega^{-0.5}$) is displayed in Fig. 9b. Our calculations showed that the diffusion coefficient of LMLO is $5.64 \times 10^{-16} \text{ cm}^2 \text{ s}^{-1}$, which is much larger than those (Table 2) of other samples. Our experiment has identified the important role of La doping on the enhancement of the structural stability and electrochemical performance of the materials.

Conclusions

Relying on a molten salt method, a series of cations were doped into Li_2MoO_3 . XRD image indicated that cation doping will not change the overall structure of LMO, while SEM and TEM results showed that the morphology of the material is changed significantly due to the doping. The incorporation of Cr^{3+} reduces the average size of particles at the most, while La^{3+} doping widens the flakes but decreases the thickness. As a result, the wide LMLO nano-sheets are formed. Furthermore, the CV tests clearly showed that many small but reversible redox pairs appear, which can be correlated to the reactions of $\text{Mo}^{(4+\delta)+}$ species caused by non-equivalent doping (M^{2+} or M^{3+}) of the samples. Due to the enhanced structural stability, the volume expansion, and the large stacking void space, LMLO sample exhibits the most promising performance. Its discharge specific capacity retains at 149.89 mAh g^{-1} after 50 cycles at a current density of 34 mA g^{-1} . The EIS test shows that the diffusion coefficient of LMLO is $5.6447 \times 10^{-16} \text{ cm}^2 \text{ s}^{-1}$, which is the largest value among all samples.

Funding information This work was financially supported by the National Natural Science Foundation of China (nos. 21773060 and 51774002), Youth Innovation Team Project of Science and Technology of Heilongjiang University (2018-KYYWF-1593), Young Scholar Project of the Long Jiang Scholars Program (Q201818), and National Defense Science and Technology Key Laboratory fund (JZX7Y201911SY009601).

References

1. Yi T-F, Wei T-T, Li Y, He Y-B, Wang Z-B (2020) Efforts on enhancing the Li-ion diffusion coefficient and electronic conductivity of titanate-based anode materials for advanced Li-ion batteries. *Energy Storage Mater* 26:165–197
2. Hsu K-F, Tsay S-Y, Hwang B-J (2004) Synthesis and characterization of nano-sized LiFePO_4 cathode materials prepared by a citric acid-based sol-gel route. *J Mater Chem* 14(17):2690–2695
3. Chen Y-Q, Xiang K-X, Zhu Y-R, Xiao L, Chen W-H, Chen X-H, Chen H (2019) Bio-template fabrication of nitrogen-doped $\text{Li}_3\text{V}_2(\text{PO}_4)_3$ /carbon composites from cattail fibers and their high-rate performance in lithium-ion batteries. *J Alloys Compd* 782:89–99
4. Zhu H, Deng W-N, Chen L, Zhang S-Y Nitrogen doped carbon layer of $\text{Li}_2\text{MnSiO}_4$ with enhanced electrochemical performance for lithium ion batteries. *Electrochim Acta* 295:956–965
5. Li Y-X, Gong Z-L, Yang Y (2007) Synthesis and characterization of $\text{Li}_2\text{MnSiO}_4/\text{C}$ nanocomposite cathode material for lithium ion batteries. *J Power Sources* 174(2):528–532
6. Lou M, Zhong H, Yu H-T, Fan S-S, Xie Y, Yi T-F (2017) $\text{Li}_{1.2}\text{Mn}_{0.54}\text{Ni}_{0.13}\text{Co}_{0.13}\text{O}_2$ hollow hierarchical microspheres with enhanced electrochemical performances as cathode material for lithium-ion battery application. *Electrochim Acta* 237:217–226
7. Yu Z (2018) Improved electrochemical performances of carbon-coated Li_2MoO_3 cathode materials for Li-ion batteries. *Int J Electrochem Sci* 64:4504–4511
8. Jang J, Kim Y, Chae OB, Yoon T, Kim SM, Kim HS, Park H, Ryu JH, Oh SM (2014) A first-cycle coulombic efficiency higher than 100% observed for a Li_2MO_3 (M=Mo or Ru) electrode. *Angew Chem Int Ed Eng* 53(40):10654–10657
9. Wang JL, Zhao Y, Zhang XQ, Wu HL, Hu SL, Wei KY, Cui YX, Su W, Cui YH (2019) Trace molybdenum doped Li_2RuO_3 as cathode material with enhanced performance for lithium ion batteries. *Sustainable Energy & Fuels* 3:2697–2704
10. Liu S, Feng X, Wang X, Shen X, Hu E, Xiao R, Yu R, Yang H, Song N, Wang Z, Yang X, Chen L (2018) Another strategy, detouring potential decay by fast completion of cation mixing. *Adv Energy Mater* 8(15):1703092
11. Kobayashi H, Tabuchi M, Shikano M, Kageyama H, Kanno R (2003) Structure, and magnetic and electrochemical properties of layered oxides, Li_2IrO_3 . *J Mater Chem* 13(4):957–962
12. Pearce PE, Perez AJ, Rouse G, Saubane M, Batuk D, Foix D, McCalla E, Abakumov AM, Van Tendeloo G, Doublet ML, Tarascon JM (2017) Evidence for anionic redox activity in a tridimensional-ordered Li-rich positive electrode beta- Li_2IrO_3 . *Nat Mater* 16(5):580–586
13. Xu C-S, Jiang W-F, Yu H-T, Guo C-F, Xie Y, Ren N, Yi T-F (2019) Hollow and hierarchical $\text{Li}_{1.2}\text{Mn}_{0.54}\text{Ni}_{0.13}\text{Co}_{0.13}\text{O}_2$ microcubes as promising cathode materials for lithium ion battery. *J Alloys Compd* 807:151686
14. Ohzuku T, Nagayama M, Tsuji K, Ariyoshi K (2011) High-capacity lithium insertion materials of lithium nickel manganese oxides for advanced lithium-ion batteries: toward rechargeable capacity more than 300 $\text{mAh}\cdot\text{g}^{-1}$. *J Mater Chem* 21(27):10179–10188
15. Ma J, Zhou Y-N, Gao Y, Yu X, Kong Q, Gu L, Wang Z, Yang X-Q, Chen L (2014) Feasibility of using Li_2moo_3 in constructing li-rich high energy density cathode materials. *Chem Mater* 26(10):3256–3262
16. Li D, He H, Wu X, Li M (2016) Electrochemical behavior of sub-micron Li_2MoO_3 as anodes in lithium-ion batteries. *J Alloys Compd* 682:759–765
17. Self EC, Zou L, Zhang M-J, Opfer R, Ruther RE, Veith GM, Song B, Wang C, Wang F, Huq A, Nanda J (2018) Synthesis and electrochemical and structural investigations of oxidatively stable Li_2MoO_3 and $x\text{Li}_2\text{MoO}_3\cdot(1-x)\text{LiMO}_2$ composite cathodes. *Chem Mater* 30(15):5061–5068
18. Ma J, Gao Y, Wang Z, Chen L (2014) Structural and electrochemical stability of Li-rich layer structured Li_2MoO_3 in air. *J Power Sources* 258:314–320
19. Hu G, Zhang M, Wu L, Peng Z, Du K, Cao Y (2016) Enhanced electrochemical performance of $\text{LiNi}_{0.5}\text{Co}_{0.2}\text{Mn}_{0.3}\text{O}_2$ cathodes produced via nanoscale coating of Li^+ -conductive Li_2SnO_3 . *Electrochim Acta* 213:547–556
20. Lou M, Fan S-S, Yu H-T, Xie Y, Zhang Q, Zhu Y-R, Yi T-F, Tian G-H (2018) Mg-doped $\text{Li}_{1.2}\text{Mn}_{0.54}\text{Ni}_{0.13}\text{Co}_{0.13}\text{O}_2$ nano flakes with

- improved electrochemical performance for lithium-ion battery application. *J Alloys Compd* 739:607–615
21. Wang C, Xu Y, Sun X, Zhang B, Chen Y, He S (2018) Enhanced electrochemical properties of F-doped $\text{Li}_2\text{MnSiO}_4/\text{C}$ for lithium ion batteries. *J Power Sources* 378:345–352
 22. Deng C, Zhang S, Yang SY, Fu BL, Ma L (2011) Synthesis and characterization of $\text{Li}_2\text{Fe}_{0.97}\text{M}_{0.03}\text{SiO}_4$ ($\text{M}=\text{Zn}^{2+}, \text{Cu}^{2+}, \text{Ni}^{2+}$) cathode materials for lithium ion batteries. *J Power Sources* 196(1):386–392
 23. Kang SH, Amine K (2005) Layered $\text{Li}(\text{Li}_{0.2}\text{Ni}_{0.15+0.5z}\text{Co}_{0.10}\text{Mn}_{0.55-0.5z})\text{O}_{2-z}\text{F}_z$ cathode materials for Li-ion secondary batteries. *J Power Sources* 146(1-2):654–657
 24. Park K-S, Im D, Benayad A, Dylla A, Stevenson KJ, Goodenough JB (2012) LiFeO_2 -incorporated Li_2MoO_3 as a cathode additive for lithium-ion battery safety. *Chem Mater* 24(14):2673–2683
 25. Yi H, Hu C, He X, Xu H (2014) Electrochemical performance of LiMnPO_4 by Fe and Zn co-doping for lithium-ion batteries. *Ionics* 21(3):667–671
 26. Yu Z, Wang X, Wan P, Zhu S, Sun Z, Zhang G, Chu W (2019) $\text{Li}_{1.233}\text{Mo}_{0.467}\text{Fe}_{0.3}\text{O}_2$ as an advanced cathode material for high-performance lithium ion battery. *Mater Lett* 249:45–48
 27. Reddy MV, Jie TW, Jafta CJ, Ozoemena KI, Mathe MK, Nair AS, Peng SS, Idris MS, Balakrishna G, Ezema FI, Chowdari BVR (2014) Studies on bare and Mg-doped LiCoO_2 as a cathode material for lithium ion batteries. *Electrochim Acta* 128:192–197
 28. Fang H, Yi H, Hu C, Yang B, Yao Y, Ma W, Dai Y (2012) Effect of Zn doping on the performance of LiMnPO_4 cathode for lithium ion batteries. *Electrochim Acta* 71:266–269
 29. Wang Y, Chen Y, Cheng S, He L (2011) Improving electrochemical performance of LiMnPO_4 by Zn doping using a facile solid state method. *Korean J Chem Eng* 28(3):964–968
 30. Feng Y, Li Y, Hou F (2009) Preparation and electrochemical properties of Cr doped LiV_3O_8 cathode for lithium ion batteries. *Mater Lett* 63(15):1338–1340
 31. Zhang S, Deng C, Fu BL, Yang SY, Ma L (2010) Effects of Cr doping on the electrochemical properties of $\text{Li}_2\text{FeSiO}_4$ cathode material for lithium-ion batteries. *Electrochim Acta* 55(28):8482–8489
 32. Wang F, Wang Y, Sun D, Wang L, Yang J, Jia H (2014) High performance $\text{Li}_2\text{MnSiO}_4$ prepared in molten KCl-NaCl for rechargeable lithium ion batteries. *Electrochim Acta* 119:131–137
 33. Luo D, Fang S, Yang L, S-i H (2017) High-rate and long-life $\text{Li}_{1.18}\text{Mn}_{0.56}\text{Ni}_{0.13}\text{Co}_{0.13}\text{O}_2$ cathodes of Li-ion batteries. *J Alloys Compd* 723:243–251
 34. Wu C, Wu F, Chen LQ, Huang XJ (2002) X-ray diffraction and X-ray photoelectron spectroscopy analysis of Cr-doped spinel LiMn_2O_4 for lithium ion batteries. *Solid State Ionics* (152-153):335-339
 35. Lee J, Urban A, Li X, Su D, Hautier G, Ceder G (2014) Unlocking the potential of cation-disordered oxides for rechargeable lithium batteries. *Science* 343:519–522
 36. Pang WK, Lee JY, Wei YS, Wu SH (2013) Preparation and characterization of Cr-doped LiMnO_2 cathode materials by Pechini's method for lithium ion batteries. *Mater Chem Phys* 139(1):241–246
 37. Chen Y, Zhao Y, An X, Liu J, Dong Y, Chen L (2009) Preparation and electrochemical performance studies on Cr-doped $\text{Li}_3\text{V}_2(\text{PO}_4)_3$ as cathode materials for lithium-ion batteries. *Electrochim Acta* 54(24):5844–5850
 38. Zhong S, Zhao B, Li Y, Liu Y, Liu J, Li F (2009) Synthesis and electrochemical properties of Cr-doped $\text{Li}_3\text{V}_2(\text{PO}_4)_3$ cathode materials for lithium-ion batteries. *J Wuhan Univ Technol Mater Sci Ed* 24(3):343–346
 39. Luo S, Tian Y, Li H, Shi K, Tang Z, Zhang Z (2010) Influence of lanthanum doping on performance of LiFePO_4 cathode materials for lithium-ion batteries. *J Rare Earths* 28(3):439–442
 40. Sun Y, Hu X, Luo W, Huang Y (2012) Ultrafine MoO_2 nanoparticles embedded in a carbon matrix as a high-capacity and long-life anode for lithium-ion batteries. *J Mater Chem* 22(2):425–431
 41. Zhao X, Cao M, Liu B, Tian Y, Hu C (2012) Interconnected core-shell MoO_2 microcapsules with nanorod-assembled shells as high-performance lithium-ion battery anodes. *J Mater Chem* 22(26):13334–13340
 42. Palanisamy K, Kim Y, Kim H, Kim JM, Yoon W-S (2015) Self-assembled porous $\text{MoO}_2/\text{graphene}$ microspheres towards high performance anodes for lithium ion batteries. *J Power Sources* 275:351–361
 43. Luo W, Hu X, Sun Y, Huang Y (2011) Electrospinning of carbon-coated MoO_2 nanofibers with enhanced lithium-storage properties. *Phys Chem Chem Phys* 13(37):16735–16740
 44. Wang C, Sun L, Zhang F, Wang X, Sun Q, Cheng Y, Wang L (2017) Formation of Mo-polydopamine hollow spheres and their conversions to MoO_2/C and $\text{Mo}_2\text{C}/\text{C}$ for efficient electrochemical energy storage and catalyst. *Small* 13(32):1701246
 45. Chen YT, Jena A, Pang WK, Peterson VK, Sheu HS, Chang H, Liu RS (2017) Voltammetric enhancement of Li-ion conduction in Al-doped $\text{Li}_{7-x}\text{La}_3\text{Zr}_2\text{O}_{12}$ solid electrolyte. *J Phys Chem C* 121(29):15565-15573
 46. Zhang JY, Zhao ZY, Wang XY, Yu T, Guan J, Yu ZT, Li ZS, Zou ZG (2010) Increasing the oxygen vacancy density on the TiO_2 surface by La-doping for dye-sensitized solar cells. *J Phys Chem C* 114:18396–18400
 47. Kumakura S, Shirao Y, Kubota K, Komaba S (2016) Preparation and electrochemical properties of $\text{Li}_2\text{MoO}_3/\text{C}$ composites for rechargeable Li-ion batteries. *Phys Chem Chem Phys* 18(41):28556–28563
 48. Yi T-F, Qiu L-Y, Mei J, Qi S-Y, Cui P, Luo S, Zhu Y-R, Xie Y, He Y-B (2020) Porous spherical $\text{NiO}@\text{NiMoO}_4@\text{PPy}$ nanoarchitectures as advanced electrochemical pseudocapacitor materials. *Sci Bull* 65(71):546–556
 49. Shi C-F, Xiang K-X, Zhu Y-R, Chen X-H, Zhou W, Chen H (2017) Preparation and electrochemical properties of nanocable-like $\text{Nb}_2\text{O}_5/\text{surface-modified carbon nanotubes}$ composites for anode materials in lithium ion batteries. *Electrochim Acta* 246(20):1088–1096
 50. He Y, Xiang K-X, Zhou W, Zhu Y-R, Chen X-H, Chen H (2018) Folded-hand silicon/carbon three-dimensional networks as a binder-free advanced anode for high-performance lithium-ion batteries. *Chem Eng J* 353:666–678

Publisher's note Springer Nature remains neutral with regard to jurisdictional claims in published maps and institutional affiliations.